Acta Materialia 199 (2020) 578–592

Contents lists available at ScienceDirect

Acta Materialia

journal homepage: www.elsevier.com/locate/actamat

Full length article

Multiaxial plasticity and fracture behavior of stainless steel 316L by laser powder bed fusion: Experiments and computational modeling

Alexander E. Wilson-Heid[a], Shipin Qin[a], Allison M. Beese[a,b,*]

[a] Department of Materials Science and Engineering, Pennsylvania State University, University Park, PA, USA
[b] Department of Mechanical Engineering, Pennsylvania State University, University Park, PA, USA

ARTICLE INFO

Article history:
Received 20 April 2020
Revised 24 August 2020
Accepted 24 August 2020
Available online 28 August 2020

Keywords:
Additive manufacturing
Powder bed fusion
Stainless steel 316L
Multiaxial plasticity and fracture
Anisotropic Hosford-Coulomb

ABSTRACT

The multiaxial large deformation and ductile fracture behavior of laser powder bed fusion (L-PBF) additively manufactured austenitic 316L stainless steel was experimentally measured. Data from tests in two orientations, under five dissimilar stress states (shear, combined shear/tension loading states, plane strain tension, and uniaxial tension) were used to calibrate and validate anisotropic plasticity and fracture models, with different specimen geometries used to probe plasticity versus fracture. Shear softening, hypothesized to be due to shear band formation in the material due to high initial dislocation density and sub-micron cellular structures, was observed in shear dominated tests, and modeled through the adoption of a shear damage criterion in an anisotropic plasticity model. Using a combined experimental and computational approach, isotropic and anisotropic Hosford-Coulomb and modified Mohr-Coulomb ductile fracture models were calibrated for both sample orientations. The calibrated anisotropic Hosford-Coulomb fracture model best captures the stress state dependent and anisotropic failure behavior of L-PBF 316L.

1. Introduction

As the field of metal additive manufacturing (AM) grows from a useful tool for fast prototyping and novelty items into a technology that transforms important industries such as aerospace, biomedical sciences, tool and die making, and many more it becomes necessary to develop a thorough understanding of the mechanical response of additively manufactured materials. Enabling load bearing applications of additively manufactured parts is in an important step for widespread adoption of the technology. Safe implementation and design against failure of additively manufactured components necessitates a description of how the materials they are built from will deform and fail under load.

While many steels have been studied for application with the layer-by-layer process of AM [1–3], austenitic 316L stainless steel (316L) is one of the most widely studied alloys in the AM industry [4]. The broad interest in the alloy stems from its current wide use in industry as a conventionally processed alloy, the ease of weldability and therefore manufacturability with AM, high corrosion and oxidation resistance, and combination of strength and elongation to failure [5,6]. The inherent rapid thermal cycling, repeated melting and solidification, of material in the AM process has been found to result in key hierarchical microstructural features including small 10–500 μm grains [7–10], fine intergranular cellular structures [9–13], and high dislocation density [7–9,12,14] that lead to an increase of yield strength relative to conventionally processed 316L. At the same time, AM introduces the risk of porosity in components – especially the laser powder bed fusion (L-PBF) technique, where the powder packing density and the optimization of other parameters such as hatch spacing for a given layer height, power, and scan speed combination are important to produce fully dense parts [15]. Porosity in additively manufactured 316L is generally from non-optimized laser parameters that result in: spherical gas entrapped pores formed during solidification [16], vapor entrapment pores from operating close to or in the keyholing mode [17,18], or lack-of-fusion (LoF) type pores with irregular morphologies at the boundaries between layers or adjacent meltpools [7,13,19–21]. The irregularly shaped LoF type pores have been found to be detrimental to mechanical properties of 316L, especially as their overall density or individual size increases [20,22,23]. The orientation dependence of the pores, where LoF pores form at the layer boundaries and their major axes are normal to the vertical build direction, contributes to the anisotropy in ductility behavior of 316L material. Ronneberg et al., found that the presence and orientation of LoF pores were correlated with a reduction of elongation to failure [7]. However, the anisotropic yield behavior was strictly a result of the microstructural features in L-PBF 316L tensile samples, such as the grain texture, columnar

* Corresponding author.
E-mail address: amb961@psu.edu (A.M. Beese).

https://doi.org/10.1016/j.actamat.2020.08.066
1359-6454/

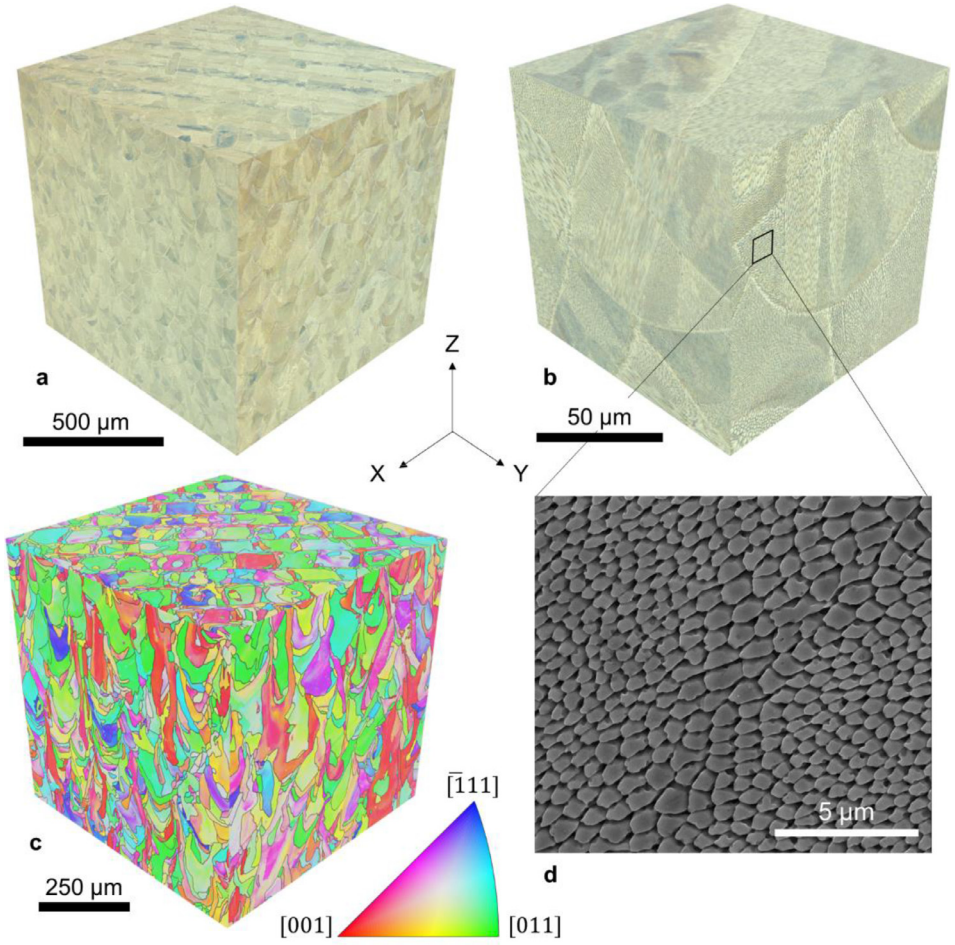

Fig. 1. (a, b) Optical micrographs showing the melt pool and grain structure in the three planes of the build. (c) EBSD images of all three planes of the build showing the epitaxial grain growth and chevron morphology of the grains in the XZ and YZ planes. For all three planes, the color shown corresponds to the hkl direction parallel to the vertical build direction (Z). (d) SEM image of the subgrain cellular structure in the XZ plane.

grain morphology and the interplay between the number of grain boundaries in each orientation and dislocation movement, and the cell growth direction due to thermal gradients during solidification [7]. It has been shown in the literature that the yield and ultimate tensile strength (UTS) is lower along the vertical build direction (BD) than the horizontal direction, referred to here as perpendicular to the build direction (⊥BD) [7,8,10,23,24]. One explanation proposed for the anisotropic strength is the solidification direction of the sub-granular cells and columnar grains [7,9,20], both of which grow along the highest thermal gradient during processing. The columnar grains can grow epitaxially through multiple layers, as shown in Fig. 1, providing statistically more grain and cell boundaries that act as dislocation barriers in the ⊥BD than BD uniaxial tension (UT) tests, resulting in increased yield strength. However, the anisotropic behavior of 316L has primarily been investigated solely under uniaxial tension, which does not provide a description of material response under other stress states.

One method for generating a more complete understanding of the elastoplastic and fracture behavior of ductile metals like 316L is to evaluate the materials under a wide range of complex stress states. The stress state dependent, multiaxial mechanical data and accompanying models that describe the behavior can then be used to design against failure in components, especially those with complex geometries allowed through the application of AM in design. It is widely understood that the strain to failure in ductile metals is stress state dependent [25–30]. Stress state can be defined as a combination of two dimensionless parameters: stress triaxiality (η) and Lode angle parameter ($\bar{\theta}$). The stress triaxiality is the ratio of the mean stress (σ_m) and von Mises equivalent stress ($\bar{\sigma}_{VM}$),

$$\eta = \frac{\sigma_m}{\bar{\sigma}_{VM}} \text{ with } \sigma_m = \frac{1}{3} I_1 \text{ and } \bar{\sigma}_{VM} = \sqrt{3 J_2} \tag{1}$$

where $I_1 = \sigma_{kk}$ is the first invariant of the stress tensor, $\boldsymbol{\sigma}$, and $J_2 = \frac{1}{2} s_{ij} s_{ij}$ is the second invariant of the deviatoric stress tensor, $\boldsymbol{s}$. The normalized Lode angle parameter is a function of the third invariant of the deviatoric stress tensor, $J_3 = det(s_{ij})$, and is defined as:

$$\bar{\theta} = 1 - \frac{2}{\pi} arccos\left[\frac{27}{2}\frac{J_3}{\bar{\sigma}_{VM}^3}\right] \tag{2}$$

Under plane stress conditions ($\sigma_3 = 0$), the relationship between the Lode angle parameter and stress triaxiality is given as:

$$\sin\left(\frac{\pi}{2}\bar{\theta}\right) = -\frac{27}{2}\eta\left(\eta^2 - \frac{1}{3}\right) \tag{3}$$

Evaluation of materials under different combinations of these two parameters is required for an accurate description of the initial yield behavior, subsequent hardening, and eventual fracture under a range of different stress states. This procedure has been used for additively manufactured materials such as L-PBF Ti-6Al-4V [31,32], Ti-6Al-4V by directed energy deposition (DED) [33,34], and stainless steel 304L by DED [35,36]. An anisotropic plasticity and fracture model was developed for L-PBF 316L by Tancogne-Dejean et al. [37]. However, due to limited data available, the model was

calibrated using only uniaxial tension and build direction double notched tension data; therefore, the authors assumed that fracture behavior was stress state independent and adopted a constant equivalent strain to fracture model.

The current study aims to address existing gaps in data with experiments and validated models that capture the effect of stress state and orientation on the plasticity and fracture behavior of L-PBF 316L. The stress state dependent plasticity and fracture behavior of this material was probed through experiments under shear, shear/tension combined loading, plane strain tension, uniaxial tension, and equibiaxial tension. The flow behavior was observed to be anisotropic in tension dominated tests, while the fracture behavior was found to be anisotropic and stress state dependent. The newly acquired experimental data, coupled with computational modeling and simulations, were used to calibrate and validate anisotropic plasticity and fracture models. The resultant models are able to capture the anisotropic flow behavior in tension dominated stress states, and the anisotropic and stress state dependent fracture behavior.

2. Experimental methods

The fabrication of the material, characterization of microstructure, and the specimens for mechanical testing used in the study are briefly summarized.

2.1. Material fabrication and characterization

The austenitic stainless steel 316L material in this study was manufactured via L-PBF AM on a 3DSystems ProX DMP 320 machine. Recycled pre-alloyed powder was used after having been sieved with a 60 μm screen. The standard 3DSystems 316L fabrication parameters for a 60 μm layer height were used: scanning speed of 900 mm/s, laser power of 300 W, and 100 μm hatch spacing. A scan strategy with outer contours and a full-length hatch fill (i.e., not checkerboard) was used for each individual component on the build plate. A 245° rotation of the hatch direction was implemented for each successive layer during the build. All microstructure characterization and mechanical testing was performed on the material in the as-built condition.

Representative samples were used for characterization of microstructure and sample density. One of the samples was sectioned into four sub-samples - one for Archimedes density analysis and three for microstructural analysis of three orthogonal planes of the material. The densities of three additional samples were analyzed with X-ray computed tomography (XCT, General Electric v|tome|x L300 nano/microCTsystem), using a voxel size of 14 µm. Following post processing in Avizo 9.3.0 software (Thermo Fisher Scientific), the samples were all found to be 99.99% dense. Archimedes density analysis, following the procedure in [22], found that samples in the study were 99.8 ± 0.1% dense. Standard metallographic procedures were used to grind and polish each microstructural subsample with a final polishing step using 0.05 μm Al_2O_3. After sample preparation, a scanning electron microscope (SEM, FEI Apreo) with an electron backscatter diffraction (EBSD, Oxford Symmetry) detector was used for grain morphology and sub-grain cell imaging, as shown in Fig. 1c and 1d, respectively. For further analysis, samples were electrolytically etched in a 10% Oxalic acid and 90% water solution at 4 V and then imaged with a digital microscope (Keyence VHX-2000), as shown in Fig. 1a-b.

The average equivalent diameter, referred to as the grain size after this point, in the XZ and YZ planes were found to be 33.6 μm and 30.0 μm, respectively, using the EBSD results. The average grain size in the XY plane was 28.2 μm.

2.2. Plasticity tests

The multiaxial plasticity behavior of the 316L material was assessed by performing mechanical tests on specimens with two different geometries, as shown in Fig. 2. The two specimen geometries allowed for the evaluation of elastoplastic properties under five different stress states. Both specimen geometries were tested in two orientations, referred to as BD and ⊥BD and schematically shown in Fig. 2. Three uniaxial tension specimens in both directions were profiled and sliced to thickness in accordance to ASTM E8 [38], from an 10 × 70 × 80 mm (thickness x width x height) wall using wire electrical discharge machining (wEDM). BD multiaxial plasticity specimens were machined from the same wall as the uniaxial tension specimens, while ⊥BD multiaxial plasticity specimens were machined from individual 3.5 × 27 × 70 mm (thickness x width x height) walls using wEDM for the outer profile and CNC milling to thickness in the gage section and grip regions.

Before testing, the gage sections for both sample types were spray painted with a white basecoat and black random speckle pattern for digital image correlation (DIC), a non-contact surface strain field measurement technique (Vic2D software, Correlated Solutions). A digital camera (Point grey GRAS-50S5M-C) was used to take an image of the gage sections during loading every one second of testing until sample failure. In multiaxial tests two identical cameras were used; one that had the entire gage region in the field of view and the other focused at the center of the gage region on the reverse side of the sample.

The uniaxial tension samples were pulled under displacement control at an applied strain rate on the order of 10^{-4} s^{-1} using an electromechanical load frame (MTS Criterion Model 43) with a 10 kN load cell. Vertical displacement was extracted from the DIC analysis with an 18 mm long virtual extensometer centered in the gage section of the uniaxial tension samples, which was used to compute strain in the vertical direction.

The geometry of the multiaxial plasticity specimens, with a thin, high aspect ratio gage section, allowed for plane stress through the thickness and plane strain along the long axis of the gage section [39]. Samples were loaded in a custom dual-actuator hydraulic test machine (MTS System Corp.), schematically shown in ref. [31]. The vertical and horizontal actuators can independently apply any combination of normal (F_V) and shear (F_H) forces to the sample. An angle β can be used to characterize the combined loading ratio as

$$\beta = \tan^{-1}\left(\frac{F_V}{F_H}\right) \tag{4}$$

In the current study four different stress states were evaluated with multiaxial plasticity specimens: shear (β=0°), shear dominated combined loading (β=30°), tension dominated combined loading (β=70°), and plane strain tension (PST, β=90°). The shear and plane strain tension tests were run in displacement control with a horizontal loading rate of 0.4 mm/min and a vertical loading rate of 0.1 mm/min, respectively. Combined loading tests were run in force control mode; for β=30°, F_H=1.5 kN/min and F_V=0.866 kN/min, and for β=70°, F_H=0.546 kN/min and F_V=1.5 kN/min. A vertical 3 mm long virtual extensometer at the center of the gage section of the plasticity sample was used to measure vertical and horizontal displacements, which were converted to vertical and in-plane shear strains [39].

This combination of experimental tests allowed for: (1) the orientation and stress state dependent elastoplastic behavior of the material to be measured, (2) the calibration and validation of a plasticity model that captured and predicted the observed behavior, and (3) the use of the plasticity model in a hybrid compu-

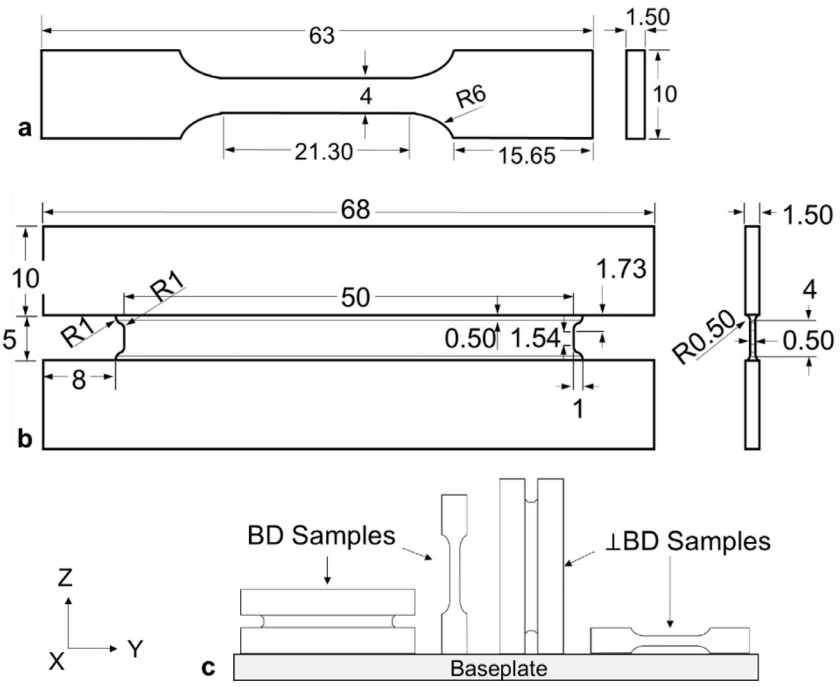

Fig. 2. (a) Uniaxial tension and (b) multiaxial plasticity specimen geometries used to evaluate the elastoplastic behavior of the L-PBF 316L material in two orientations – BD (tension along the z-axis) and ⊥BD (tension along the y-axis). Units in mm. (c) Schematic of the sample orientations and nomenclature with respect to the baseplate, not to scale.

tational/experimental approach to quantify the multiaxial fracture behavior of L-PBF 316L, as discussed in upcoming sections.

2.3. Fracture tests

The onset of fracture of L-PBF 316L for a wide range of stress states was studied through experiments on samples extracted in two orientations. The three different geometries used to study fracture were selected because under applied macroscopic deformation, the strain in these geometries localizes at predictable locations, which is where failure is assumed to initiate. These locations for each sample geometry are shown in Fig. 3: the surface of the hole in central hole tension samples, the inside center of the butterfly samples, and the center top surface of the punch samples. Note that under pure shear, failure may initiate at the edges of the butterfly sample before the sample fails at the center. However, as the central point in the butterfly sample during this loading remains under a constant state of shear throughout loading, using the strain at the center of the specimen up to the moment of specimen failure provides a lower bound for damage to failure under shear. The applied displacement to onset of failure was recorded in each experiment.

For sample fabrication, central hole (CH) tension specimens in both directions were profiled and sliced to thickness with wEDM from a 10 × 70 × 80 mm wall (thickness x width x height), with the central hole drilled and then cut to size with wEDM. Multiaxial fracture specimens, referred to as butterfly specimens [40], were machined with the same process as that for the plasticity specimens from individual 3.5 × 34 × 80 mm (thickness x width x height) walls in both orientations. An extruded punch sample geometry was directly manufactured and sliced to thickness with wEDM for the punch tests.

In central hole tension, a uniaxial tension stress state is maintained throughout nearly the entire test at the edge of the central hole along the centerline of the specimen normal the loading direction. Three central hole tension samples in each build orientation were loaded on the same load frame as the uniaxial tension samples in Section 2.2 with a loading rate of 0.0162 mm/s. A 10 mm virtual extensometer was used at the center of the gage section to measure displacement to onset of failure in the tests, defined by the first visual identification of a crack.

The butterfly geometry featured a reduced thickness gage region similar to the plasticity specimens, as well as a non-uniform gage height such that fracture is assumed to start at the center of the shortest region of the gage section at half through-thickness [40]. Using DIC, with the camera focused on the center of the gage section, the displacement at the onset of failure was recorded for two samples of each stress state and build orientation. The butterfly samples were tested using the same custom load frame as the multiaxial plasticity specimens and using the same loading angles, β.

The fracture behavior of L-PBF 316L was also observed under equibiaxial tension with a punch experiment. The punch test is widely used [41–44], and the experimental set-up is identical to that presented in ref. [32] in which a disk specimen is fixed in a die, and impacted with a hemispherical punch during quasistatic loading. For the punch experiments, three-dimensional DIC was used to measure the surface deformation field during loading up to the onset of failure (Vic3D, Correlated Solutions). Displacement up to failure was measured using the crosshead displacement with an assumed compliance of 19 kN/mm.

The displacements to onset of fracture from the experiments presented in this section were used in the calibration and validation of a ductile fracture model for L-PBF 316L. The wide range of tests performed provide important information for understandings the orientation and stress state dependent ductile fracture behavior of L-PBF 316L.

3. Plasticity behavior: experimental results and model

The experimental findings of tests probing plasticity behavior, and their use in the calibration and validation of a plasticity model are presented in this section. Differences between experimental results and the finite element analysis (FEA) simulations of these

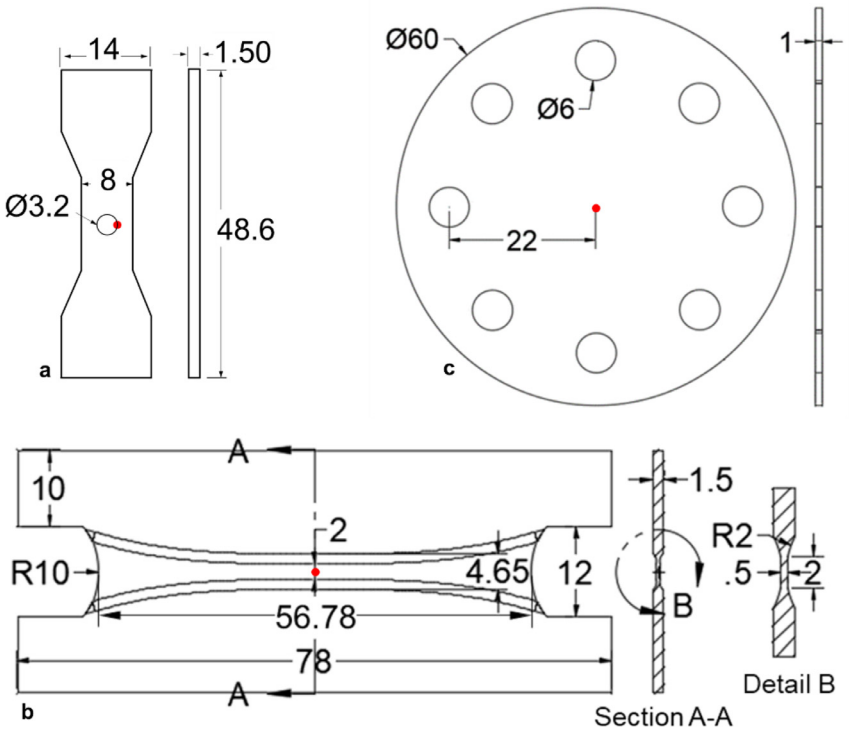

Fig. 3. (a) Central hole tension and (b) butterfly specimens used to evaluate the fracture behavior of the L-PBF 316L material in two orientations – BD (tension along the z-axis) and ⊥BD (tension along the y-axis). (c) Equibiaxial tension specimens that were fabricated in the x-y plane, and loaded out of plane (along the build axis). Red circles indicate the locations at which fracture is assumed to initiate, where the location is at the through-thickness center in (a) and (b) and on the top surface in (c). Units in mm.

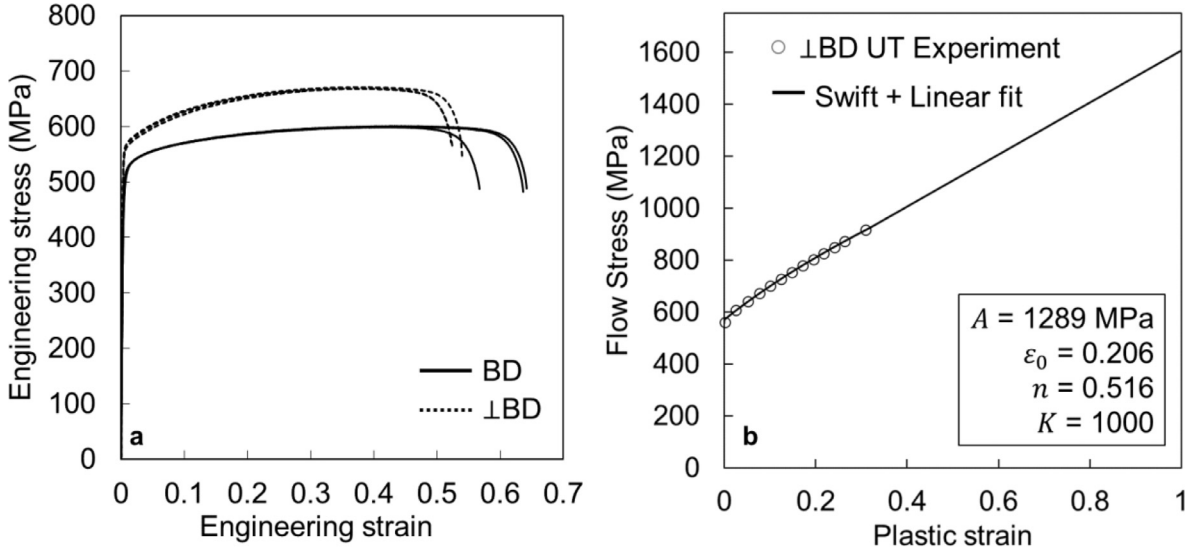

Fig. 4. (a) Engineering stress-strain data for uniaxial tension in both orientations. (b) Flow versus plastic strain for a representative ⊥BD uniaxial tension test along with a Swift law fit prior to necking, and a linear extrapolation after necking.

using the plasticity model are discussed with respect to the microstructure and defects present in the L-PBF 316L material.

3.1. Experimental results

3.1.1. Uniaxial tension results

The engineering stress-strain behavior for the six uniaxial tension tests, three in each orientation, agreed well with the direction-dependent trends observed in the literature, as shown in Fig. 4. The yield strength (⊥BD: 558 ± 3 MPa and BD: 497 ± 8 MPa) and UTS (⊥BD: 670 ± 1 MPa and BD: 600 ± 1 MPa) were greater in the ⊥BD orientations samples than BD samples. The ductility of the material was also anisotropic, BD samples had higher engineering strain to failure than ⊥BD samples, 62 ± 3% and 53 ± 1%, respectively. The anisotropic strength in the L-PBF 316L is hypothesized to have originated from the microstructural features, most notably the columnar grain morphology that creates more barriers for dislocation motion in the ⊥BD loaded samples, that were observed in our material and the literature [7,8].

3.1.2. Multiaxial plasticity results

The multiaxial plasticity tests revealed mixed isotropic and anisotropic behavior dependent on stress state, as shown in Fig. 5. Tension dominated loading conditions, plane strain tension and

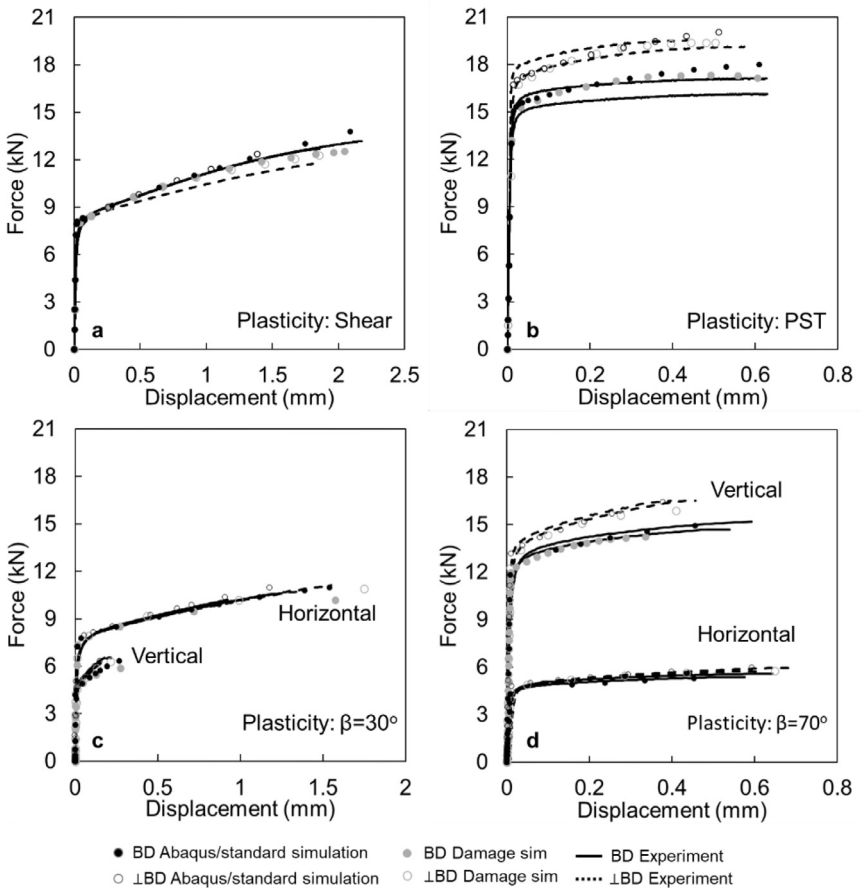

Fig. 5. Comparison of experimental (symbols) and simulated (lines) force versus displacement curves for (a) pure shear, (b) plane strain tension (c) combined loading with β=30°, and (d) combined loading with β=60° in both orientations. The mechanical response in the tension dominated tests show notable anisotropy.

β=70°, had similar behavior as seen under uniaxial tension in which larger vertical force was applied to the ⊥BD samples compared to BD samples to achieve the same displacement. The force versus displacement behavior in shear dominated tests, shear and β=30°, was isotropic. The anisotropic, stress state dependent behavior of the material was similar to the behavior observed in L-PBF Ti-6Al-4V [31], except that the L-PBF 316L was significantly more ductile. All stress states except plane strain tension and β=70° in the ⊥BD reached an equivalent plastic strain of ≥20%. Based on similar anisotropic experimental behavior observed in the two studies a plasticity model using the same framework as that in ref. [31] was initially implemented with calibration of new model parameters for L-PBF 316L, as discussed in the next section.

3.2. Plasticity modeling

3.2.1. Hardening model

To describe the hardening behavior of the material, a Swift law with linear extrapolation after necking was used. The hardening behavior is represented in the form of a piecewise function as:

$$\Delta\sigma_y = \begin{cases} nA(\varepsilon_0 + \bar{\varepsilon}^p)^{n-1}\,\Delta\bar{\varepsilon}^p & \bar{\varepsilon}^p \le 0.032 \\ K\Delta\bar{\varepsilon}^p & \bar{\varepsilon}^p > 0.032 \end{cases} \quad (5)$$

where σ_y is the flow stress, $\bar{\varepsilon}_p$ is the equivalent plastic strain, and A, ε_0, n, and K are material constants. The constants were calibrated for a representative ⊥BD uniaxial tension test, and are given in Table 1. The ⊥BD was chosen to be the reference orientation for the model as it would be minimally influenced by any potential LoF defects. A comparison between experimental data and the calibrated model is given in Fig. 4.

Table 1
Calibrated plasticity model parameters.

Swift law parameters	A (MPa)	ε_0	n	K(MPa)
	1289	0.206	0.516	1000
Hill48 parameters	F	G	H	
	0.63	0.42	0.58	
	N	L	M	
	1.58	1.6	1.6	

3.2.2. Yield function and flow rule

The Hill 1948 anisotropic yield function (Hill48) [45] was implemented to capture the multiaxial plasticity behavior of L-PBF 316L. The yield function is given as:

$$f = \sigma_{\text{Hill48}} - \sigma_y = 0 \quad (6)$$

where σ_y is the current yield stress, and the equivalent Hill48 stress, σ_{Hill48}, under the plane stress condition is defined as:

$$\sigma_{\text{Hill48}} = \sqrt{F(\sigma_{22}-\sigma_{33})^2 + G(\sigma_{33}-\sigma_{11})^2 + H(\sigma_{11}-\sigma_{22})^2 + 2L\sigma_{23}{}^2 + 2M\sigma_{31}{}^2 + 2N\sigma_{12}{}^2} \quad (7)$$

where F, G, H, L, M, and N are constants that describe the material's anisotropy, σ_{11} and σ_{22} are the normal stresses along the ⊥BD and BD directions, respectively, and σ_{23}, σ_{31}, and σ_{12} are

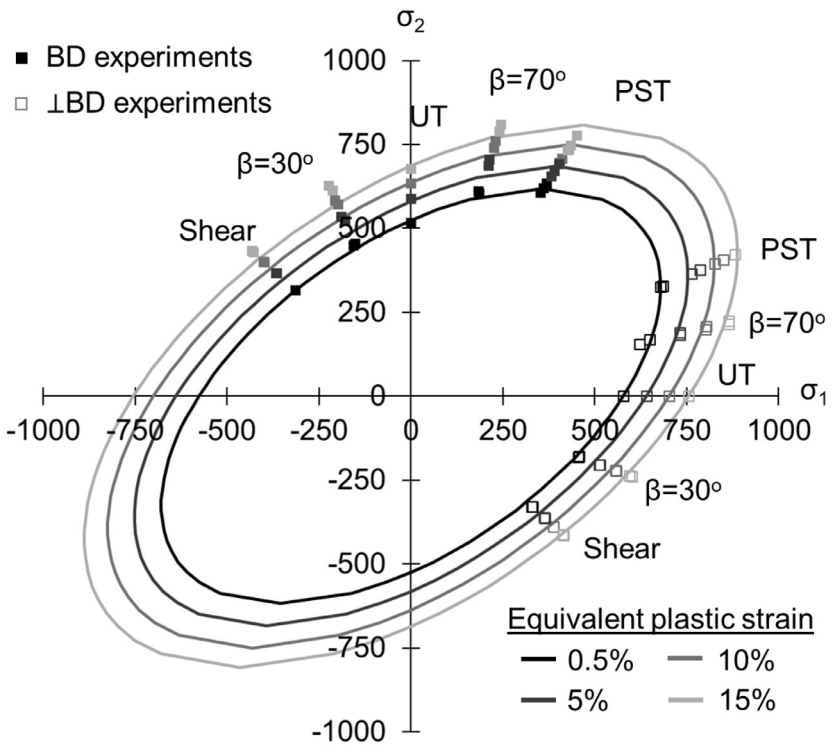

Fig. 6. Anisotropic Hill48 2D yield surface (for plane stress) at initial yield (0.5% Hill48 equivalent plastic strain) and subsequent increments of strain up to 15% for L-PBF 316L. The yield surfaces are shown as lines, while experimental data are shown as symbols.

the shear stress components. Assuming an associated flow rule, the plastic strain increment can be calculated as:

$$\dot{\varepsilon}_{ij}^{p} = \dot{\gamma}\frac{\partial f(\sigma_{ij})}{\partial \sigma_{ij}} \tag{8}$$

where $\dot{\gamma}$ is the plastic multiplier. The equivalent plastic strain, $\bar{\varepsilon}_{\text{Hill48}}^{p}$, is defined as the accumulation of $\dot{\gamma}$, i.e., $\bar{\varepsilon}_{\text{Hill48}}^{p} = \int_0^t d\gamma$, and its relationship with the plastic strain components is given through the following incremental form:

$$d\bar{\varepsilon}_{\text{Hill48}}^{p} = \sqrt{\frac{F\left(d\varepsilon_{11}^{p}\right)^2 + G\left(d\varepsilon_{22}^{p}\right)^2 + H\left(d\varepsilon_{33}^{p}\right)^2}{FG+FH+GH} + \frac{2\left(d\varepsilon_{23}^{p}\right)^2}{L} + \frac{2\left(d\varepsilon_{31}^{p}\right)^2}{M} + \frac{2\left(d\varepsilon_{12}^{p}\right)^2}{N}} \tag{9}$$

3.2.3. Model calibration

The model in Eqn. (7) was calibrated with experimental data from uniaxial tension, shear, and β=70° plasticity tests. Additionally, $G + H$ was assumed to be equal to 1 because the strain hardening parameters were calibrated along the σ_{11} or ⊥BD orientation. Using the uniaxial tension initial yield data along the two orientations $F + H$ was calculated to be 1.21, and L and M were both calculated to be 1.6. To calibrate N, σ_{Hill48} was computed for the initial yield under uniaxial tension in the ⊥BD direction and set equal to $\sigma_{\text{Hill48}} = \sqrt{2N(\sigma_{12}^{y})^2}$, where σ_{12}^{y} was the average yield stress in shear tests, resulting in $N = 1.58$. With all other model parameters calibrated except H, Eqn. (7) was used with the average β=70° initial yield stress components (σ_{11}, σ_{22}, and σ_{12}) from both orientations, which resulted in a calibrated value of $H = 0.58$.

3.2.4. Model validation

The Hill48 yield surface and comparison with experiments for each stress state in both orientations is shown in Fig. 6. The initial yield surface (0.5% equivalent plastic strain) agrees well with all the experimental data in both orientations, including those tests not used in calibration of the model parameters, β=30° and plane strain tension. Subsequent surfaces that represent the evolution of the Hill48 equivalent plastic strain are also shown in Fig. 6. The model does well to capture the entire set of experimental data in for the ⊥BD tests; however, the model does not capture the BD plane strain tension experimental data as well after initial yield. The model slightly overpredicts the experimental σ_{Hill48} (average difference of 7%) with increased plastic strain for BD plane strain tension, as shown by the mismatch between the 15% evolved Hill48 equivalent plastic strain surface and the last experimental data point in Fig. 6. This result can be explained when considering the effect of voids in the high stress triaxiality regime (for plane strain tension, η=0.58) where the voids are being opened in two directions – along the vertical applied tension direction and the horizontal direction due to the stress resulting from zero strain along the gage width – having a larger reduction of strain to failure compared to other tests with a shear stress component and reduced σ_{22}.

The model was implemented into the commercial finite element analysis software Abaqus using the implicit solver [46]. To check the ability of the model to capture and predict the experimentally measured data, half-thickness multiaxial plasticity specimens were modeled and discretized into 14,336 C3D8R type elements, with a symmetry boundary condition applied along the

sample thickness plane. The top and bottom grips were defined as rigid bodies, and each grip was tied to a reference node. All degrees of freedom of the bottom reference node were constrained. For the shear and plane strain tension tests, a displacement was applied to the top grip reference node in the horizontal and vertical directions, respectively. The combined loading tests were simulated using force vectors applied to the top node corresponding to the representative β angle. Force data were extracted from the top reference node in simulations. Horizontal and vertical displacement data were extracted from two nodes, one 3 mm above the other, in the center of the gage section on the modeled sample surface, identical to the experimental DIC virtual extensometers. Fig. 5 compares the force vs. displacement response in each of the simulations with their experimental counterparts. The calibrated and validated plasticity model captured the orientation and stress state dependent plasticity tests in the current study, even for those tests that were not used in the calibration of the model. The largest discrepancy was observed in the ⊥BD shear test, where the maximum force was 13% larger in the simulation than in the experiments.

4. Fracture behavior: experimental results and model

The quantification of ductile strain to failure requires a well calibrated plasticity model, implemented in an FEA framework, for simulating stress state and plastic strain evolution to failure in fracture experiments. The procedure for quantifying the stress state dependent strain to failure and calibrating a suitable ductile fracture model is discussed in this section.

4.1. Experimental results

4.1.1. Central hole tension results

The force vs. displacement results for the four central hole tension tests, two in each orientation, are shown in Fig. 7. The maximum force in the ⊥BD sample was 11% greater than measured in the BD tests. The displacement to failure was similar in three of the four tests, while one of the BD tests had higher strain to failure. These tests showed the same anisotropy as observed in the tension dominated plasticity tests, namely that the ⊥BD samples required higher forces for the same deformation.

4.1.2. Butterfly results

A total of sixteen butterfly tests were completed, two replications for each combination of orientation and stress state. An anisotropic force vs. displacement response was observed in the tension dominated butterfly tests, while the shear dominated tests were isotropic, as shown in Fig. 7. The differences in the maximum force at fracture for the vertical force component in the plane strain tension and β=70° tests were 15% and 14%, respectively.

4.1.3. Punch results

The experimentally measured force vs. displacement curves for five tests are shown in Fig. 7. The largest percent difference between any two tests for maximum force and displacement to failure was 7% and 2%, respectively. The principal stresses in the punch tests were out of plane relative to the BD and ⊥BD orientations of all other samples; therefore, these tests were used in calibration of the fracture surfaces for both orientations.

4.2. Fracture modeling

4.2.1. Finite element modeling

To probe the evolution of stress triaxiality, Lode angle parameter, stress and plastic strain components, and equivalent plastic strain to failure in each fracture test in this study, a simulation of each test, using Abaqus/implicit, was performed using the calibrated plasticity model presented in Section 3. The evolution of stress state parameters and equivalent plastic strain were extracted from the locations denoted in Fig. 3, which were assumed to be the locations of failure initiation in each geometry. Mesh size dependence studies were performed for all three geometries such that the mesh size was decreased by half until the computed strain to failure changed by less than 3% between subsequent simulations.

For the central hole tension tests, a 1/8th model geometry, with 136,448 C3D8R elements, was used. Symmetry boundary conditions were applied on each of the three cut planes, and a vertical displacement boundary was applied to a reference node that controlled the vertical displacement of all nodes. A half-thickness butterfly geometry was modeled with 738,241 C3D8R elements. Similar to the simulations of the plasticity specimens in Section 3.2.4, the grips were modeled as rigid, and the same displacement or force boundary conditions were used up to the experimentally observed displacement to failure. Punch tests were simulated with a full thickness, ¼ disk specimen geometry using 627,900 C3D8R and 3588 C3D6R type elements for the disk specimen with all degrees of freedom constrained along the circumference of the disk and symmetry boundary conditions on the cut planes. The hemispherical punch and die were modeled as a rigid body analytical surfaces with a coefficient of friction of zero between the surfaces and the disk specimen. A vertical displacement boundary condition, using the same displacement needed for experimental failure, was applied to the punch, while the top die was fixed in all degrees of freedom.

Experimentally measured and computationally simulated force vs. displacement behavior were compared for each test. In the central hole and butterfly simulations, force was extracted from the top reference node and the displacements were extracted from nodes corresponding to the ends of the experimentally used virtual extensometers. The force and displacement in the punch simulations were extracted from the node at the apex of the rigid hemispherical punch, where the punch first contacted the disk specimen.

In the shear dominated tests (shear and β=30°), the strain hardening behavior in the simulations exceeds that observed experimentally, resulting in a large divergence from experimental results at high strain. At the same time, there was very good agreement between simulations and experiments in the tension dominated stress states (plane strain tension and β=70°). To better capture the behavior of the shear dominated butterfly tests, a damage initiation model was implemented. Damage models have been used to describe the influence of cracks and texture in L-PBF 316L in the literature [47], although ref. [47] used elements of crystal plasticity and only studied how the microscale features imparted damage in ⊥BD uniaxial tension tests. Here, the built-in shear damage initiation model in Abaqus was used, in order to capture in shear dominated tests without impacting the tension dominated simulations.

The shear damage initiation criterion in Abaqus is a phenomenological model based on damage initiating from shear band localization [46]. The equivalent plastic strain at the onset of damage in the model is dependent on the equivalent plastic strain rate ($\dot{\bar{\varepsilon}}_p$) and shear stress ratio χ_s:

$$\chi_s = \frac{(\bar{\sigma}_{VM} + k_s\sigma_m)}{\tau_{max}} \tag{10}$$

where k_s is a material parameter and τ_{max} is the maximum shear stress. Calibrated values of $k_s = 0.3$ and $\chi_s = 1.73$ at an equivalent plastic strain of 10% for damage initiation were determined through a parametric study. The criterion for damage initiation is

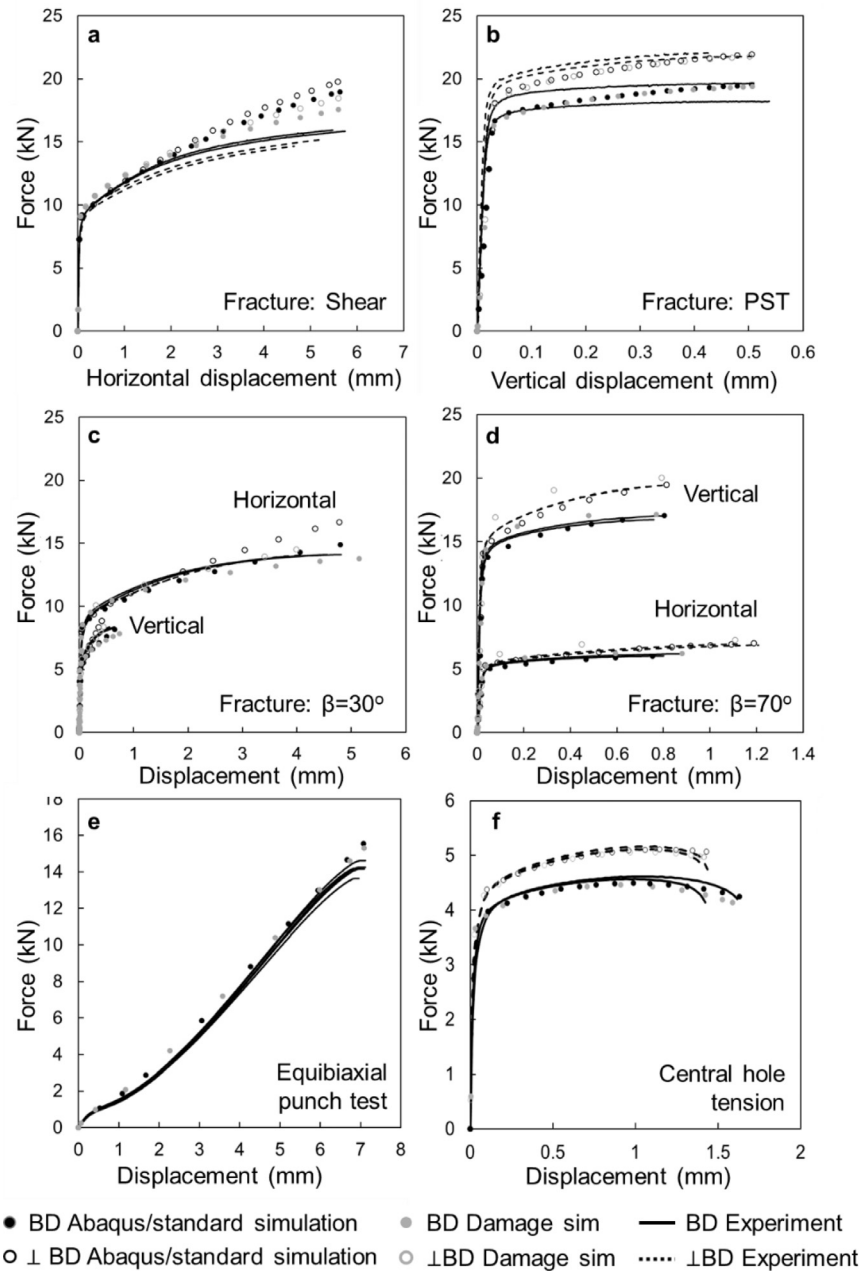

Fig. 7. Comparison of fracture geometry experimental and simulated force versus displacement curves for (a) pure shear, (b) plane strain tension (c) combined loading with β=30°, (d) combined loading with β=60°, (e) equibiaxial tension, and (f) central hole tension in two orientations.

met when:

$$w_s = \int \frac{d\bar{\varepsilon}_p}{\bar{\varepsilon}_p\left(\chi_s,\ \dot{\bar{\varepsilon}}_p\right)} = 1 \tag{11}$$

where the state variable w_s increases monotonically with plastic deformation [46]. Once the damage initiation criterion was met, a linear damage evolution plus linear softening was adopted to implement a reduction in flow stress (compared to damage-free material) with accumulated plastic strain. The standard linear softening model in Abaqus was calibrated to capture the observed force vs. displacement experimental behavior under shear.

For simulations involving damage, Abaqus/explicit was used. For all models, a mass scaling factor was used to reduce simulation time while ensuring that the kinetic energy of the model was no greater than 5% of the total internal energy. The force vs. displacement results for each of the fracture test simulations with damage is shown in Fig. 7. With the implementation of damage, the β=30° simulation agreed very well with the experiments and the pure shear simulation agreed better, but still has a force difference at failure of 9.8% and 19% in the BD and ⊥BD orientations, respectively. Using the standard model with no consideration of damage the force difference at failure was 18% and 26% for the BD and ⊥BD orientations, respectively. The incorporation of the damage did not influence the tension dominated fracture simulations and was also reincorporated to the plasticity type simulations with no effect, as shown in Fig. 5.

In annealed stainless steel 316L, thermal softening due to the formation of adiabatic shear bands has been observed experimentally under shear loading at high strain rates [48,49]. Xue and Gray showed that a high defect density resulting in subgrain structures was a prerequisite for shear localization, and once deformation localized in shear bands, the local temperature in those shear bands

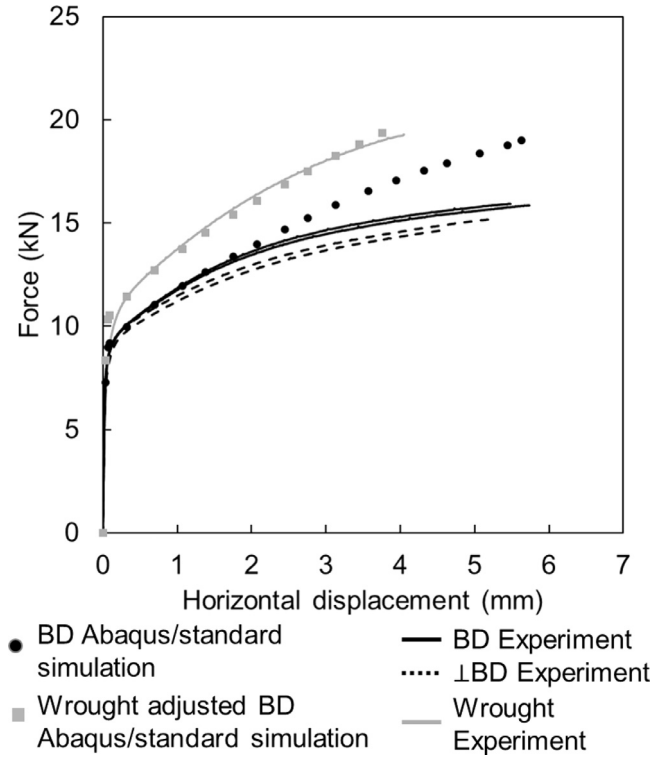

Fig. 8. Comparison of the shear fracture geometry force vs. displacement experimental behavior of rolled austenitic stainless steel 316 sheet and L-PBF 316L material. The force of the calibrated Abaqus/Standard simulation without damage was increased by 15% to match the rolled experimental behavior and the comparison shows that the rolled material does not undergo shear softening.

was calculated to increase by 470 °C. Together the formation of the shear band and temperature increase resulted in softening. Softening from shear bands formed under quasi-static loading for iron has also been reported, but only for grain sizes below 300 nm [50]. For the present shear fracture tests of L-PBF 316L, a maximum temperature increase of only 9.6 °C was measured using an infrared camera (Optris PI300 and Optris PIX Connect software) during testing, thus, adiabatic shear banding was ruled out in these tests. In as-built L-PBF 316L the dislocation density has been found to be orders of magnitude larger than that observed in annealed rolled material [14]. Additionally, the sub granular cells, measuring 0.5 to 1 μm in smallest dimension [11,13], are partially responsible for increased yield strength in this material. Therefore, it is hypothesized that the initial large defect density fulfills the prerequisite of high defect density, and the sub granular cells provide significant boundaries for dislocation motion, similar to grain refinement, such that even at quasi-static strain rates the shear band localization occurs in L-PBF 316L.

A comparison of the experimental force versus displacement behavior of rolled austenitic stainless steel 316 sheet and the L-PBF material under pure shear loading using the butterfly geometry is shown in Fig. 8. Adjusting the standard simulation (no damage) plasticity model to account for the initial offset in flow stress in the rolled sheet versus the L-PBF material shows that unlike the L-PBF material, the rolled material does not exhibit shear softening. The microstructural features therefore justify the application of the phenomenological shear damage initiation criterion in the computational material model.

4.2.2. Calibration of fracture models

The evolution of the equivalent plastic strain up to failure as a function of the two stress state parameters is shown in Fig. 9 and

Table 2
Average values of the strain to failure, stress triaxiality, and Lode angle parameter for each test performed. These values were used for MMC model calibration and validation.

Sample Type	Orientation	# of tests	Avg. $\bar{\varepsilon}_f$	Avg. η	Avg. $\bar{\theta}$
Central Hole	BD	2	1.04	0.33	0.94
	⊥BD	2	0.96	0.34	0.98
Shear	BD	2	0.88	−0.02	−0.05
	⊥BD	2	0.76	0.01	0.02
β30	BD	2	0.84	0.17	0.49
	⊥BD	2	0.71	0.18	0.51
β70	BD	2	0.38	0.49	0.40
	⊥BD	2	0.39	0.47	0.46
PST	BD	2	0.22	0.60	−0.15
	⊥BD	2	0.22	0.57	0.06
Punch	–	5	0.72	0.68	−0.84

a summary of the average value of each stress state parameter up to fracture is given in Table 2. The fracture behavior of the material exhibited an orientation dependence, and the strains to fracture along BD were larger than their counterparts along PBD for most of the loading types, with the only exception being β=70° and PST. Therefore, an anisotropic fracture model was needed to describe the fracture behavior. In the current study, the anisotropic Hosford-Coulomb (HC) model [51] and the anisotropic modified Mohr-Coulomb (MMC) fracture model [52] were adopted. In what follows, the definition of both models will be recalled briefly, while references [51,52] provide further details.

For both models, a damage indicator, D, is calculated as:

$$D = \int_0^{\bar{\varepsilon}} \frac{1}{\bar{\varepsilon}_f^{pr}} \, d\bar{\varepsilon}_{frac}^{p} \tag{12}$$

where $\bar{\varepsilon}_f^{pr}$ is a model-dependent weighting function, and $\bar{\varepsilon}_{frac}^{p}$ is a model-dependent equivalent plastic strain. $D = 0$ for the virgin material, and it gradually increases with plastic deformation. The material is regarded to be failed when $D = 1$.

For the anisotropic HC model, $\bar{\varepsilon}_{frac}^{p}$ is the equivalent plastic strain defined in the plasticity model, which is the Hill48 equivalent plastic strain in the current case (Eqn. (9)), and the weighting function $\bar{\varepsilon}_f^{pr}$ is defined as:

$$\bar{\varepsilon}_f^{pr}(\boldsymbol{M\sigma}/\bar{\sigma}) = b\left(\frac{1+c}{g_{HC}\left(\frac{\boldsymbol{M\sigma}}{\bar{\sigma}}\right)}\right)^{\frac{1}{d}} \tag{13}$$

where b, c and d are model parameters, $\bar{\sigma}$ is the von Mises equivalent stress, and $\boldsymbol{\sigma}$ is the Cauchy stress tensor. In the current study, $\boldsymbol{\sigma}$ is expressed in Voigt notation as $[\sigma_{11}, \sigma_{22}, \sigma_{33}, \sigma_{12}, \sigma_{23}, \sigma_{31}]$. $\boldsymbol{M}$ is a linear transformation matrix defined as:

$$\boldsymbol{M} = \begin{bmatrix} 1 & M_{12} & 0 & 0 & 0 & 0 \\ 0 & M_{22} & 0 & 0 & 0 & 0 \\ 0 & 0 & 1 & 0 & 0 & 0 \\ 0 & 0 & 0 & M_{44} & 0 & 0 \\ 0 & 0 & 0 & 0 & 1 & 0 \\ 0 & 0 & 0 & 0 & 0 & 1 \end{bmatrix} \tag{14}$$

where M_{12}, M_{22}, and M_{44} are transformation coefficients that must be calibrated, and g_{HC} is a function of the normalized stress tensor $\boldsymbol{\sigma}/\bar{\sigma}$, which is in turn a function of η and $\bar{\theta}$:

$$g_{HC}\left(\frac{\boldsymbol{\sigma}}{\bar{\sigma}}\right) = \left\{\frac{1}{2}\left[(f_1 - f_2)^a + (f_2 - f_3)^a + (f_1 - f_3)^a\right]\right\}^{\frac{1}{a}} + c(2\eta + f_1 + f_3) \tag{15}$$

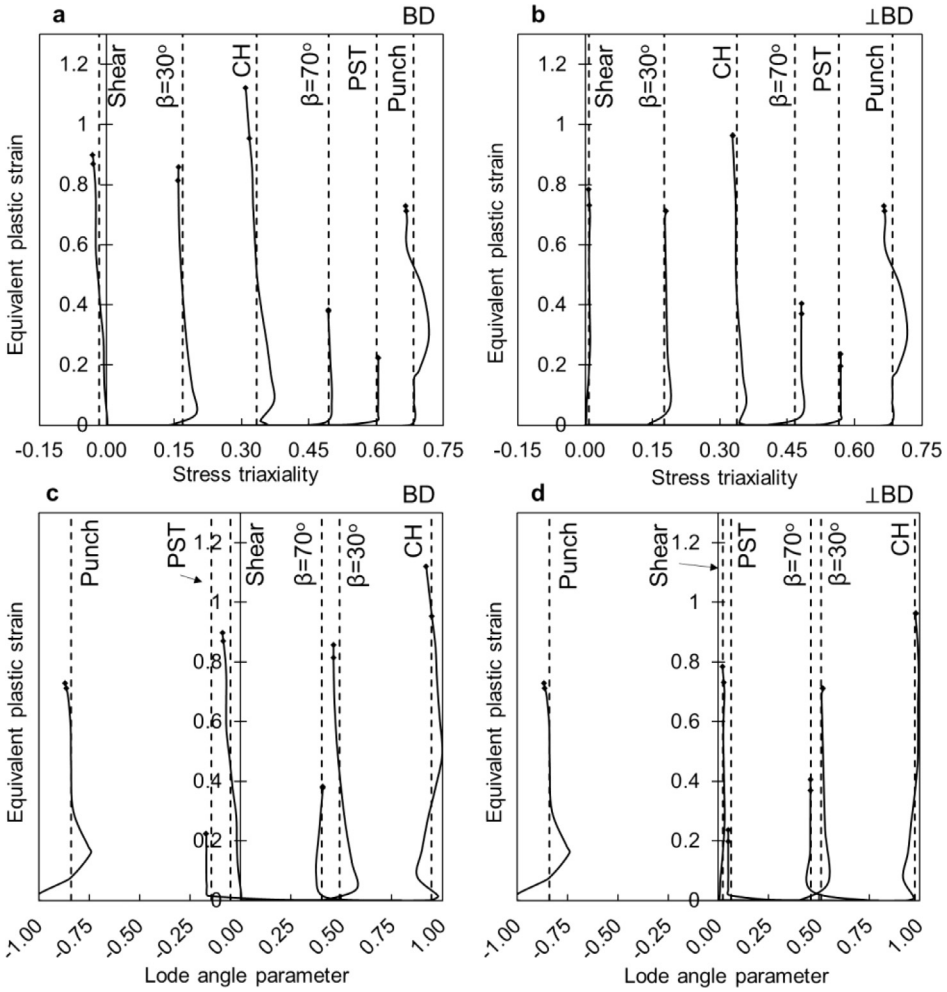

Fig. 9. Evolution of the (a, b) stress triaxiality and (c, d) Lode angle parameter (solid lines) up to failure (symbols) for each sample geometry in both the BD (a, c) and ⊥BD (b, d) directions with the average value of each stress state parameter used in fracture model calibration represented by a vertical dashed line.

where a is a model parameter, and f_1, f_2, and f_3 are defined as:

$$f_1 = \frac{2}{3}\cos\left[\frac{\pi}{6}\left(1-\bar{\theta}\right)\right]$$
$$f_2 = \frac{2}{3}\cos\left[\frac{\pi}{6}\left(3+\bar{\theta}\right)\right] \quad (16)$$
$$f_3 = -\frac{2}{3}\cos\left[\frac{\pi}{6}\left(1+\bar{\theta}\right)\right]$$

By applying the transformation matrix $\boldsymbol{M}$ to the stress tensor $\boldsymbol{\sigma}$, g_{HC} is changed from an isotropic function of $\boldsymbol{\sigma}$ to an anisotropic function of $\boldsymbol{\sigma}$, thus making the fracture model anisotropic.

For the anisotropic MMC model, the weighting function $\bar{\varepsilon}_f^{pr}$ is defined as:

$$\bar{\varepsilon}_f^{pr} = \left\{\frac{A}{c_2}\left[c_\theta^s + \frac{\sqrt{3}}{2-\sqrt{3}}\left(1-c_\theta^s\right)\left(\sec\left(\frac{\bar{\theta}\pi}{6}\right)-1\right)\right]\right.$$
$$\left.\left[\sqrt{\frac{1+c_1^2}{3}}\cos\left(\frac{\bar{\theta}\pi}{6}\right)+c_1\left(\eta+\frac{1}{3}\sin\left(\frac{\bar{\theta}\pi}{6}\right)\right)\right]\right\}^{-\frac{1}{n}} \quad (17)$$

where A and n are hardening parameters (the same variables presented in Eqn. (5)), and c_1, c_2, and c_θ^s are model parameters [32,53].

The anisotropic MMC model uses an equivalent plastic strain definition that is independent of the plasticity model. Luo et al. adopted two equivalent plastic strain definitions for the MMC model: one that was equivalent to that in the plasticity model and one that was independent of the plasticity model [52]. They showed that the model accuracy was higher when adopting an equivalent plastic strain definition that was independent of the plasticity model. Following the framework in ref. [52], the equivalent plastic strain for the anisotropic MMC model is defined as:

$$\bar{\varepsilon}_{frac}^p = \sqrt{\frac{2}{3}\left[\boldsymbol{\beta}\cdot(d\boldsymbol{\varepsilon}_p)\right]\cdot\left[\boldsymbol{\beta}\cdot(d\boldsymbol{\varepsilon}_p)\right]} \quad (18)$$

where $\boldsymbol{\varepsilon}_p$ is the plastic strain tensor expressed in Voigt notation as $[\varepsilon_{11}^p, \varepsilon_{22}^p, \varepsilon_{33}^p, \sqrt{2}\varepsilon_{12}^p, \sqrt{2}\varepsilon_{23}^p, \sqrt{2}\varepsilon_{31}^p]$, and $\boldsymbol{\beta}$ is a linear transformation matrix defined as:

$$\boldsymbol{\beta} = \begin{bmatrix} 1 & 0 & 0 & 0 & 0 & 0 \\ 0 & \beta_{22} & 0 & 0 & 0 & 0 \\ 0 & 0 & \beta_{33} & 0 & 0 & 0 \\ 0 & 0 & 0 & \beta_{44} & 0 & 0 \\ 0 & 0 & 0 & 0 & 1 & 0 \\ 0 & 0 & 0 & 0 & 0 & 1 \end{bmatrix} \quad (19)$$

where β_{22}, β_{33}, and β_{44} are transformation coefficients that must be calibrated.

To summarize, the parameters to be calibrated for the anisotropic HC model are: *a, b, c, d,* M_{12}, M_{22}, and M_{44}, and those for the anisotropic MMC model are c_1, c_2, c_θ^s, β_{22}, β_{33}, and β_{44}. In the current study, a Matlab code was developed to determine the parameter values. The code optimized the parameter values using

Table 3
Calibrated anisotropic and isotropic HC and MMC model parameters.

Hosford-Coulomb	a	b	c	d	M_{12}	M_{22}	M_{44}
Anisotropic	0.970	1.184	0.127	0.091	−0.032	0.961	1.347
Isotropic - BD	0.694	1.300	0.244	0.199			

Modified Mohr-Coulomb	c_1	c_2 (MPa)	c_θ^s	β_{22}	β_{33}	β_{44}
Anisotropic	0.860	1372	2.102	0.618	−0.461	−0.084
Isotropic - BD	1.150	1923	1.871			

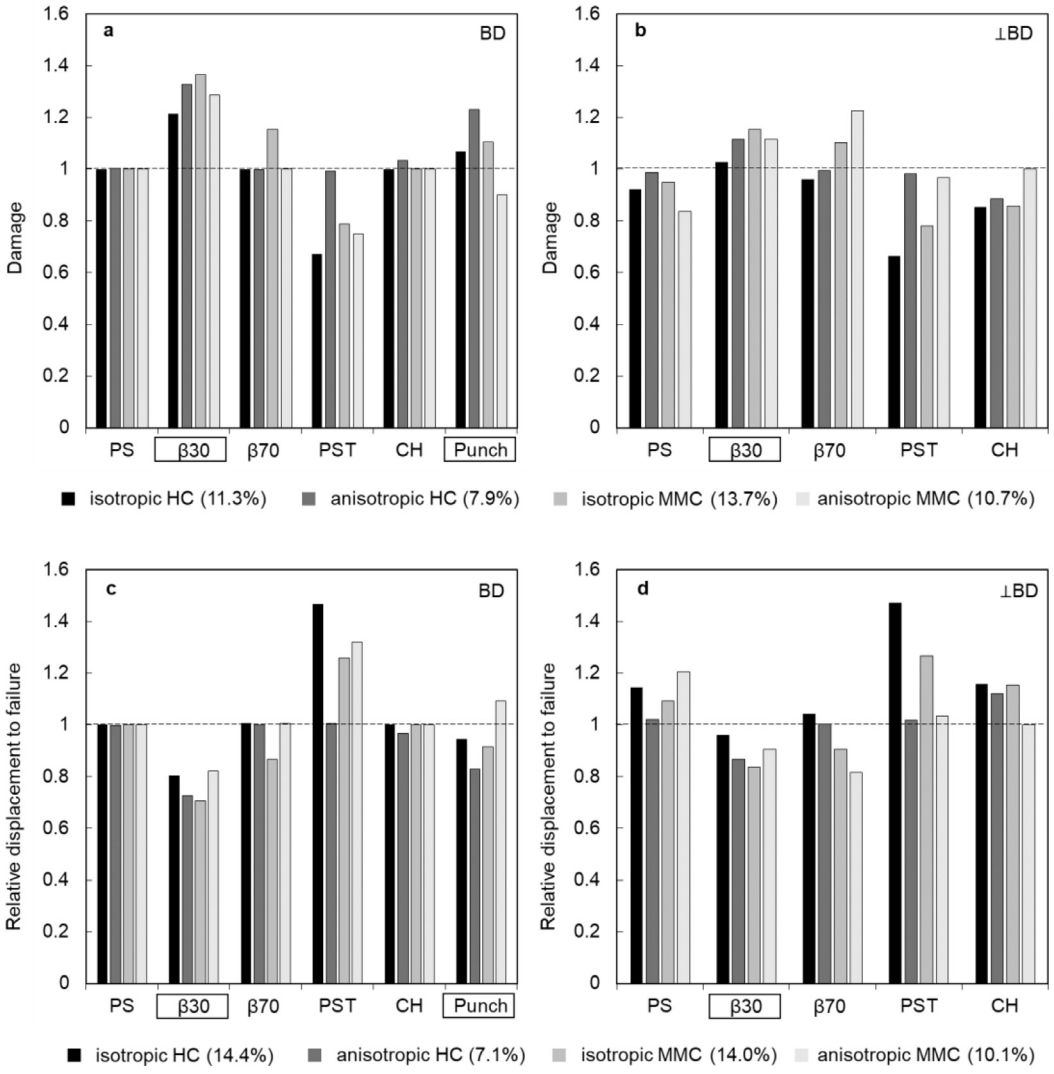

Fig. 10. (a,b) Damage accumulation at fracture and (c,d) relative displacement to failure comparisons of the four different fracture models: isotropic HC, anisotropic HC, isotropic MMC, and anisotropic MMC. In the legends, the value in parenthesis indicates the mean absolute percentage error between the specified model predictions for each stress state studied in both orientations and a value of 1. The boxed x-axes labels indicate tests that were not used in calibration of the models.

the interior-point algorithm so that the resultant D values in the experiments used for calibration were as close to 1 as possible at the moment of fracture. For the anisotropic HC and MMC models, the tests used for calibration were: pure shear, β=70°, plane strain tension, and central hole tension, leaving punch and β=30° for model validation. The calibrated parameter values are summarized in Table 3.

Further, the isotropic variations of the HC and MMC models were calibrated in each orientation independently [30,41]. The isotropic HC model is obtained by setting the $\boldsymbol{M}$ matrix in the anisotropic HC model to the identity matrix. The isotropic MMC model is obtained by replacing the equivalent plastic strain definition in the anisotropic MMC model (Eqn. (18)) with that in the plasticity model (i.e., $\bar{\varepsilon}^p_{frac} = \bar{\varepsilon}^p_{\text{Hill48}}$). Using the same calibration tests and procedure, but only for the build direction tests, a direct comparison was made with the anisotropic models. The calibrated parameters for each model are given in Table 3.

4.2.3. Results and discussion of fracture models

Using the calibrated parameter values, the accumulated damage at the moment of fracture (D) for each of the tests are shown in Fig. 10. The isotropic versions of the HC and MMC fracture models, calibrated with the build direction tests, resulted in a mean absolute percentage error (MAPE) for damage prediction across all tests in both orientations of 11.3% and 13.7% for the HC and MMC models, respectively. The MAPE values for the HC and MMC mod-

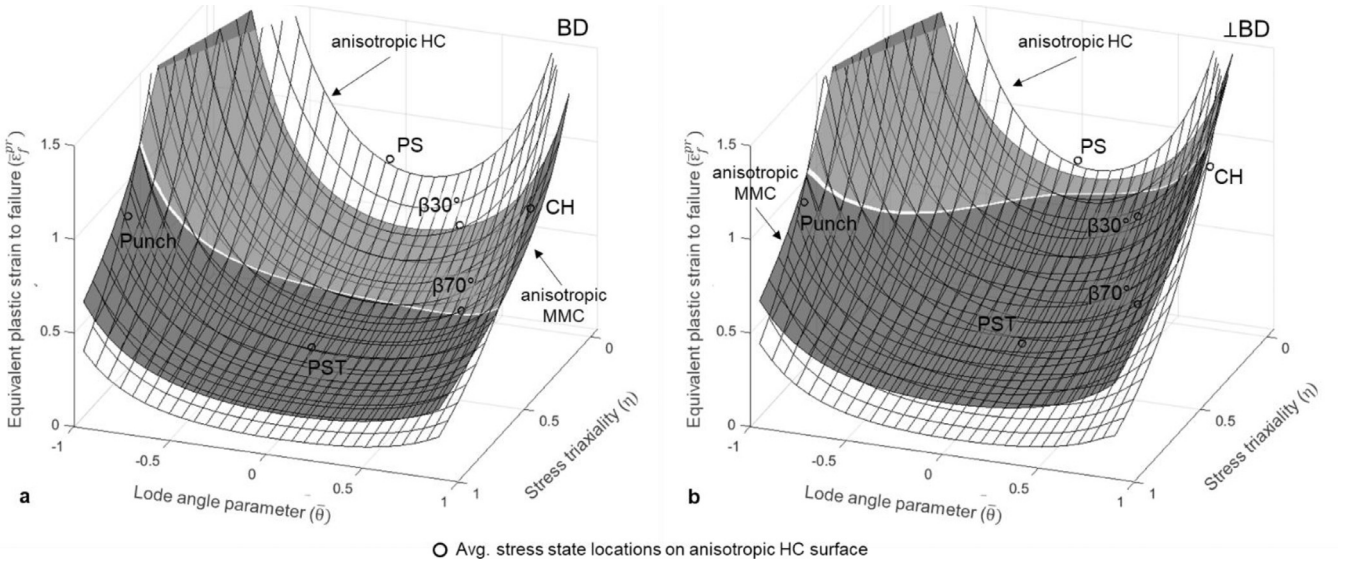

Fig. 11. Schematic comparisons of the anisotropic HC and MMC fracture surfaces in three-dimensional space of stress triaxiality vs. Lode angle parameter vs. equivalent plastic strain to failure for the (a) build direction and (b) perpendicular build direction samples. Symbols indicate the locations of each stress state directly on the anisotropic HC surface at the average location of the stress triaxiality and Lode angle parameter for each stress state under assumed proportional loading. Damage accumulates slower at locations where the surface is higher for each model.

els were reduced when adopting the anisotropic variations of each model, although the anisotropic HC model resulted in the lowest amount of error of all the models calibrated. This finding indicates that the anisotropic HC model best captures the multiaxial failure behavior of L-PBF 316L.

The relative displacement to failure values, defined as the predicted displacement to failure divided by the measured displacement to failure, for each model are also shown in Fig. 10. Note that in almost all cases, the relative displacement to failure is below 1, indicating that the calibrated models are largely conservative when predicting failure under the stress states considered. For example, the least agreement between the anisotropic HC model and experimental data was for β=30°, where the average displacement to failure for samples in the BD was found to be 4.69 mm in experiments, while the model predicted failure at a displacement of 3.41 mm, 73% of the experimental value.

To visualize the differences between the anisotropic HC model and the anisotropic MMC model, the fracture surfaces along BD and ⊥BD for both models are shown in Fig. 11. In the plots, the maximum principal stress direction was assumed to be aligned with the BD or ⊥BD, and the minimum principal stress direction was assumed to be aligned with the thickness direction. Note that the fracture surfaces in the figure can be interpreted as the fracture strain limit for the condition of proportional loading. In actual tests, in which the loading paths are typically nonproportional, the fracture surfaces should be interpreted as the reciprocal of the damage accumulation rate (i.e., the higher the fracture surface, the slower damage accumulates).

The fracture surfaces of both models have the same general shape, but the anisotropic HC model shows higher sensitivity to both η and $\bar{\theta}$, which explains why the anisotropic HC model was able to better capture the experimental data compared to the anisotropic MMC model. The higher stress state sensitivity of the anisotropic HC model comes from its dependence on all three principal stresses, while the anisotropic MMC model depended on the first and third principal stresses only [41].

5. Summary and conclusions

The isotropic and anisotropic HC and MMC ductile fracture models were calibrated for L-PBF 316L in two orientations. The anisotropic HC model was able to accurately capture and predict the experimental data in the present study. In general, the L-PBF 316L exhibited more anisotropy in strength than ductility, but only for tension dominated loading conditions. The major findings of the study are as follows:

- Anisotropic initial yield strength behavior, hypothesized to derive from grain morphology effects, was only observed in the tension dominated tests, which most directly probed the difference in grain dimensions along loading different orientations.
- The plasticity behavior of L-PBF 316L was found to be stress state dependent and somewhat anisotropic. The proposed plasticity model consisting of an anisotropic Hill48 initial yield criterion, associated flow rule, and isotropic hardening equation captured the large deformation experimental results for a wide range of stress states.
- Shear softening, hypothesized to be due to shear band formation in shear dominated experiments, was captured through the implementation of a shear damage criterion in the plasticity model. With the calibrated damage initiation and linear softening, agreement between experiments and simulations was improved for shear dominated stress states and had no effect on the tension dominated stress states.
- The ductile fracture behavior of L-PBF 316L was found to depend strongly on stress state and slightly on build direction. The experimental data were used to calibrate the anisotropic Hosford-Coulomb fracture model, which captured the accumulated damage at the moment of fracture and relative displacement to failure within 7.9% and 7.1% mean absolute percentage error, respectively, for L-PBF 316L.

Declaration of Competing Interest

The authors declare that they have no known competing financial interests or personal relationships that could have appeared to influence the work reported in this paper.

The authors declare the following financial interests/personal relationships which may be considered as potential competing interests.

Acknowledgements

The financial support provided by the National Science Foundation through award number CMMI-1652575 is gratefully acknowledged. Any opinions, findings, and conclusions or recommendations expressed in this material are those of the authors and do not necessarily reflect the views of the National Science Foundation. The samples were fabricated at Penn State's Center for Innovative Materials Processing through Direct Digital Deposition (CIMP-3D).

Supplementary materials

Supplementary material associated with this article can be found, in the online version, at doi:10.1016/j.actamat.2020.08.066.

References

[1] A.T. Polonsky, W.C. Lenthe, M.P. Echlin, V. Livescu, G.T. Grayiii, T.M. Pollock, Solidification-driven Orientation Gradients in Additively Manufactured Stainless Steel, Acta Mater. (2019), doi:10.1016/j.actamat.2019.10.047.
[2] Z. Wang, T.A. Palmer, A.M. Beese, Effect of processing parameters on microstructure and tensile properties of austenitic stainless steel 304L made by directed energy deposition additive manufacturing, Acta Mater 110 (2016) 226–235, doi:10.1016/j.actamat.2016.03.019.
[3] T. LeBrun, T. Nakamoto, K. Horikawa, H. Kobayashi, Effect of Retained Austenite on Subsequent Thermal Processing and Resultant Mechanical Properties of Selective Laser Melted 17-4 PH Stainless Steel, Mater Des. (2015), doi:10.1016/j.matdes.2015.05.026.
[4] P. Bajaj, A. Hariharan, A. Kini, P. Kürnsteiner, D. Raabe, E.A. Jägle, Steels in additive manufacturing: a review of their microstructure and properties, Mater Sci Eng A 772 (2020), doi:10.1016/j.msea.2019.138633.
[5] S.D. Washko, G. Aggen, ASM Handbook, in: Properties and Selection: Irons, Steels, and High-Performance Alloys, 1990, pp. 841–907.
[6] T. DebRoy, H.L. Wei, J.S. Zuback, T. Mukherjee, J.W. Elmer, J.O. Milewski, A.M. Beese, A. Wilson-Heid, A. De, W. Zhang, Additive manufacturing of metallic components – Process, structure and properties, Prog Mater Sci 92 (2018) 112–224, doi:10.1016/j.pmatsci.2017.10.001.
[7] T. Ronneberg, C.M. Davies, P.A. Hooper, Revealing relationships between porosity, microstructure and mechanical properties of laser powder bed fusion 316L stainless steel through heat treatment, Mater Des. (2020), doi:10.1016/j.matdes.2020.108481.
[8] Y.-D. Im, K.-H. Kim, K.-H. Jung, Y.-K. Lee, K.-H. Song, Anisotropic Mechanical Behavior of Additive Manufactured AISI 316L Steel, Metall Mater Trans A. (2019), doi:10.1007/s11661-019-05139-7.
[9] Z. Sun, X. Tan, S.B. Tor, C.K. Chua, Simultaneously enhanced strength and ductility for 3D-printed stainless steel 316L by selective laser melting, NPG Asia Mater 10 (2018) 127–136, doi:10.1038/s41427-018-0018-5.
[10] J. Suryawanshi, K.G. Prashanth, U. Ramamurty, Mechanical behavior of selective laser melted 316L stainless steel, Mater Sci Eng A 696 (2017) 113–121, doi:10.1016/j.msea.2017.04.058.
[11] Y. Zhong, L. Liu, S. Wikman, D. Cui, Z. Shen, Intragranular cellular segregation network structure strengthening 316L stainless steel prepared by selective laser melting, J Nucl Mater 470 (2016) 170–178, doi:10.1016/j.jnucmat.2015.12.034.
[12] Z. Li, T. Voisin, J.T. McKeown, J. Ye, T. Braun, C. Kamath, W.E. King, Y.M. Wang, Tensile properties, strain rate sensitivity, and activation volume of additively manufactured 316L stainless steels, Int J Plast. (2019), doi:10.1016/j.ijplas.2019.05.009.
[13] U. Scipioni Bertoli, B.E. MacDonald, J.M. Schoenung, Stability of cellular microstructure in laser powder bed fusion of 316L stainless steel, Mater Sci Eng A 739 (2019) 109–117, doi:10.1016/J.MSEA.2018.10.051.
[14] M.S. Pham, B. Dovgyy, P.A. Hooper, Twinning induced plasticity in austenitic stainless steel 316L made by additive manufacturing, Mater Sci Eng A 704 (2017) 102–111, doi:10.1016/j.msea.2017.07.082.
[15] S. Sun, M. Brandt, M. Easton, Powder bed fusion processes: an overview, Laser Additive Manufacturing (2017) 55–77.
[16] B. Zhang, Y. Li, Q. Bai, Defect Formation Mechanisms in Selective Laser Melting: a Review, Chinese J Mech Eng 30 (2017) 515–527, doi:10.1007/s10033-017-0121-5.
[17] W.E. King, H.D. Barth, V.M. Castillo, G.F. Gallegos, J.W. Gibbs, D.E. Hahn, C. Kamath, A.M. Rubenchik, Observation of keyhole-mode laser melting in laser powder-bed fusion additive manufacturing, J Mater Process Technol 214 (2014) 2915–2925, doi:10.1016/j.jmatprotec.2014.06.005.
[18] S.A. Khairallah, A.T. Anderson, A. Rubenchik, W.E. King, Laser powder-bed fusion additive manufacturing: physics of complex melt flow and formation mechanisms of pores, spatter, and denudation zones, Acta Mater 108 (2016) 36–45, doi:10.1016/j.actamat.2016.02.014.
[19] H. Choo, K.-L. Sham, J. Bohling, A. Ngo, X. Xiao, Y. Ren, P.J. Depond, M.J. Matthews, E. Garlea, Effect of laser power on defect, texture, and microstructure of a laser powder bed fusion processed 316L stainless steel, Mater Des (2018) 1–12, doi:10.1016/j.matdes.2018.12.006.
[20] E. Garlea, H. Choo, C.C. Sluss, M.R. Koehler, R.L. Bridges, X. Xiao, Y. Ren, B.H. Jared, Variation of elastic mechanical properties with texture, porosity, and defect characteristics in laser powder bed fusion 316L stainless steel, Mater Sci Eng A (2019) 138032, doi:10.1016/j.msea.2019.138032.
[21] T. Larimian, M. Kannan, D. Grzesiak, B. AlMangour, T. Borkar, Effect of energy density and scanning strategy on densification, microstructure and mechanical properties of 316L stainless steel processed via selective laser melting, Mater Sci Eng A 770 (2020) 138455, doi:10.1016/j.msea.2019.138455.
[22] A.E. Wilson-Heid, T.C. Novak, A.M. Beese, Characterization of the Effects of Internal Pores on Tensile Properties of Additively Manufactured Austenitic Stainless Steel 316L, Exp Mech. (2018), doi:10.1007/s11340-018-00465-0.
[23] R. Casati, J. Lemke, M. Vedani, Microstructure and Fracture Behavior of 316L Austenitic Stainless Steel Produced by Selective Laser Melting, J Mater Sci Technol 32 (2016) 738–744, doi:10.1016/j.jmst.2016.06.016.
[24] S.L.B. Kramer, A. Jones, A. Mostafa, et al., The third Sandia fracture challenge: predictions of ductile fracture in additively manufactured metal, Int J Frac 218 (2019) 5–61, doi:10.1007/s10704-019-00361-1.
[25] F.A. McClintock, A Criterion for Ductile Fracture by the Growth of Holes, J Appl Mech 35 (1968) 363–371.
[26] A.L. Gurson, Continuum Theory of Ductile Rupture by Void Nucleation and Growth: part I—Yield Criteria and Flow Rules for Porous Ductile Media, J Eng Mater Technol 99 (1977) 2, doi:10.1115/1.3443401.
[27] G.R. Johnson, W.H. Cook, A constitutive model and data for metals subjected to large strains, high strain rates and high temperatures, in: 7th Int. Symp. Ballist., 1983, pp. 541–547.
[28] M.S. Mirza, D.C. Barton, P. Church, The effect of stress triaxiality and strain-rate on the fracture characteristics of ductile metals, J Mater Sci 31 (1996) 453–461, doi:10.1007/BF01139164.
[29] Y. Bao, T. Wierzbicki, On fracture locus in the equivalent strain and stress triaxiality space, Int J Mech Sci 46 (2004) 81–98, doi:10.1016/j.ijmecsci.2004.02.006.
[30] Y. Bai, T. Wierzbicki, A new model of metal plasticity and fracture with pressure and Lode dependence, Int J Plast 24 (2008) 1071–1096, doi:10.1016/j.ijplas.2007.09.004.
[31] A.E. Wilson-Heid, S. Qin, A.M. Beese, Anisotropic multiaxial plasticity model for laser powder bed fusion additively manufactured Ti-6Al-4V, Mater Sci Eng A 738 (2018) 90–97, doi:10.1016/j.msea.2018.09.077.
[32] A.E. Wilson-Heid, A.M. Beese, Fracture of laser powder bed fusion additively manufactured Ti–6Al–4V under multiaxial loading: calibration and comparison of fracture models, Mater Sci Eng A (2019) 137967, doi:10.1016/j.msea.2019.05.097.
[33] M.B. Gorji, T. Tancogne-Dejean, D. Mohr, Heterogeneous random medium plasticity and fracture model of additively-manufactured Ti-6Al-4V, Acta Mater 148 (2018) 442–455, doi:10.1016/j.actamat.2018.02.025.
[34] T. Tancogne-Dejean, C.C. Roth, U. Woy, D. Mohr, Probabilistic fracture of Ti-6Al-4V made through additive layer manufacturing, Int J Plast 78 (2016) 145–172, doi:10.1016/j.ijplas.2015.09.007.
[35] Z. Wang, A.M. Beese, Stress state-dependent mechanics of additively manufactured 304L stainless steel: part 2 – Characterization and modeling of macroscopic plasticity behavior, Mater Sci Eng A 743 (2019) 824–831, doi:10.1016/j.msea.2018.11.091.
[36] Z. Wang, A.M. Beese, Stress state-dependent mechanics of additively manufactured 304L stainless steel: part 1 – characterization and modeling of the effect of stress state and texture on microstructural evolution, Mater Sci Eng A 743 (2019) 811–823, doi:10.1016/j.msea.2018.11.094.
[37] T. Tancogne-Dejean, M.B. Gorji, K. Pack, C.C. Roth, The third Sandia Fracture Challenge: deterministic and probabilistic modeling of ductile fracture of additively-manufactured material, Int J Fract. (2019), doi:10.1007/s10704-019-00355-z.
[38] ASTM International (2016) E8/E8M -16a: standard Test Methods for Tension Testing of Metallic Materials
[39] D. Mohr, M. Oswald, A New Experimental Technique for the Multi-axial Testing of Advanced High Strength Steel Sheets, Exp Mech 48 (2008) 65–77, doi:10.1007/s11340-007-9053-9.
[40] M. Dunand, D. Mohr, Optimized butterfly specimen for the fracture testing of sheet materials under combined normal and shear loading, Eng Fract Mech 78 (2011) 2919–2934, doi:10.1016/j.engfracmech.2011.08.008.
[41] D. Mohr, S.J. Marcadet, Micromechanically-motivated phenomenological Hosford-Coulomb model for predicting ductile fracture initiation at low stress triaxialities, Int J Solids Struct 67-68 (2015) 40–55, doi:10.1016/j.ijsolstr.2015.02.024.
[42] C.C. Roth, D. Mohr, Ductile fracture experiments with locally proportional loading histories, Int J Plast 79 (2016) 328–354, doi:10.1016/j.ijplas.2015.08.004.
[43] M. Dunand, D. Mohr, Hybrid experimental-numerical analysis of basic ductile fracture experiments for sheet metals, Int J Solids Struct 47 (2010) 1130–1143, doi:10.1016/j.ijsolstr.2009.12.011.
[44] S. Qin, A.M. Beese, Multiaxial fracture of DP600: experiments and finite element modeling, Materials Science and Enginering A 785 (2020) 1–9, doi:10.1016/j.msea.2020.139386.
[45] R. Hill, A Theory of the Yielding and Plastic Flow of Anisotropic Metals, Proc R Soc A Math Phys Eng Sci 193 (1948) 281–297, doi:10.1098/rspa.1948.0045.
[46] Simulia (2016) Abaqus User Manual v2016
[47] M. Taheri Andani, M. Ghodrati, M.R. Karamooz-Ravari, R. Mirzaeifar, J. Ni, Damage modeling of metallic alloys made by additive manufacturing, Mater Sci Eng A 743 (2019) 656–664, doi:10.1016/j.msea.2018.11.125.

[48] Q. Xue, I.T. Gray, Development of adiabatic shear bands in annealed 316L stainless steel: part II. TEM studies of the evolution of microstructure during deformation localization, Metall Mater Trans A Phys Metall Mater Sci 37 (2006) 2447–2458, doi:10.1007/BF02586218.

[49] Q. Xue, I.T. Gray, Development of adiabatic shear bands in annealed 316L stainless steel: part I. Correlation between evolving microstructure and mechanical bahavior, Metall Mater Trans A Phys Metall Mater Sci 37 (2006) 2435–2446, doi:10.1007/BF02586217.

[50] D. Jia, K.T. Ramesh, E. Ma, Effects of nanocrystalline and ultrafine grain sizes on constitutive behavior and shear bands in iron, Acta Mater 51 (2003) 3495–3509, doi:10.1016/S1359-6454(03)00169-1.

[51] G. Gu, D. Mohr, Anisotropic Hosford-Coulomb fracture initiation model: theory and application, Eng Fract Mech 147 (2015) 480–497, doi:10.1016/j.engfracmech.2015.08.004.

[52] M. Luo, M. Dunand, D. Mohr, Experiments and modeling of anisotropic aluminum extrusions under multi-axial loading - Part II: ductile fracture, Int J Plast 32-33 (2012) 36–58, doi:10.1016/j.ijplas.2011.11.001.

[53] Y. Bai, T. Wierzbicki, Application of extended Mohr-Coulomb criterion to ductile fracture, Int J Fract 161 (2010) 1–20, doi:10.1007/s10704-009-9422-8.